The Journal of Chemical Physics

Hyperspectral CARS microscopy and quantitative unsupervised analysis of deuterated and non-deuterated fatty acid storage in human cells

Cite as: J. Chem. Phys. **155**, 224202 (2021); https://doi.org/10.1063/5.0065950
Submitted: 06 August 2021 • Accepted: 14 November 2021 • Accepted Manuscript Online: 15 November 2021 • Published Online: 08 December 2021

Dale Boorman, Iestyn Pope, Francesco Masia, et al.

COLLECTIONS

Paper published as part of the special topic on Chemical Imaging

View Online Export Citation CrossMark

ARTICLES YOU MAY BE INTERESTED IN

Toward photoswitchable electronic pre-resonance stimulated Raman probes
The Journal of Chemical Physics **154**, 135102 (2021); https://doi.org/10.1063/5.0043791

Visualization of intracellular lipid metabolism in brown adipocytes by time-lapse ultra-multiplex CARS microspectroscopy with an onstage incubator
The Journal of Chemical Physics **155**, 125102 (2021); https://doi.org/10.1063/5.0063250

Ultrahigh-speed multiplex coherent anti-Stokes Raman scattering microspectroscopy using scanning elliptical focal spot
The Journal of Chemical Physics **155**, 144201 (2021); https://doi.org/10.1063/5.0063987

Challenge us.
What are your needs for periodic signal detection?
Watch

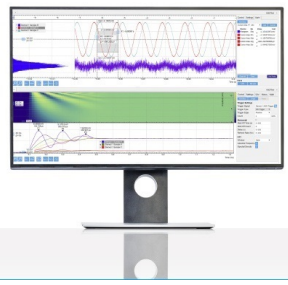

Zurich Instruments

© 2021 Author(s).

AIP Publishing

The Journal of Chemical Physics ARTICLE scitation.org/journal/jcp

Hyperspectral CARS microscopy and quantitative unsupervised analysis of deuterated and non-deuterated fatty acid storage in human cells

Cite as: J. Chem. Phys. 155, 224202 (2021); doi: 10.1063/5.0065950
Submitted: 6 August 2021 • Accepted: 14 November 2021 •
Published Online: 8 December 2021

View Online Export Citation CrossMark

Dale Boorman,[1] Iestyn Pope,[1] Francesco Masia,[1,2] Wolfgang Langbein,[2] Steve Hood,[3] Paola Borri,[1] and Peter Watson[1,a)]

AFFILIATIONS

[1] School of Biosciences, Sir Martin Evans Building, Cardiff University, Museum Avenue, Cardiff CF10 3AX, United Kingdom
[2] School of Physics and Astronomy, Cardiff University, The Parade, Cardiff CF24 3AA, United Kingdom
[3] GSK Medicines Research Centre, Gunnels Wood Road, Stevenage, Hertfordshire SG1 2NY, United Kingdom

Note: This paper is part of the JCP Special Topic on Chemical Imaging.
[a)] **Author to whom correspondence should be addressed:** WatsonPD@cardiff.ac.uk

ABSTRACT

Coherent anti-Stokes Raman scattering (CARS) implemented as a vibrational micro-spectroscopy modality eradicates the need for potentially perturbative fluorescent labeling while still providing high-resolution, chemically specific images of biological samples. Isotopic substitution of hydrogen atoms with deuterium introduces minimal change to molecular structures and can be coupled with CARS microscopy to increase chemical contrast. Here, we investigate HeLa cells incubated with non-deuterated or deuterium-labeled fatty acids, using an in-house-developed hyperspectral CARS microscope coupled with an unsupervised quantitative data analysis algorithm, to retrieve Raman susceptibility spectra and concentration maps of chemical components in physically meaningful units. We demonstrate that our unsupervised analysis retrieves the susceptibility spectra of the specific fatty acids, both deuterated and non-deuterated, in good agreement with reference Raman spectra measured in pure lipids. Our analysis, using the cell-silent spectral region, achieved excellent chemical specificity despite having no prior knowledge and considering the complex intracellular environment inside cells. The quantitative capabilities of the analysis allowed us to measure the concentration of deuterated and non-deuterated fatty acids stored within cytosolic lipid droplets over a 24 h period. Finally, we explored the potential use of deuterium-labeled lipid droplets for non-invasive cell tracking, demonstrating an effective application of the technique for distinguishing between cells in a mixed population over a 16 h period. These results further demonstrate the chemically specific capabilities of hyperspectral CARS microscopy to characterize and distinguish specific lipid types inside cells using an unbiased quantitative data analysis methodology.

Published under an exclusive license by AIP Publishing. https://doi.org/10.1063/5.0065950

INTRODUCTION

Biological systems are chemically complex, and thus, the ability to distinguish a molecule of interest in a heterogeneous chemical environment presents an ongoing challenge within cell biology and pharmacological sciences. An ideal imaging modality would achieve high spatial resolution with three-dimensional sectioning capabilities and quantitative chemical specificity, with minimal structural change imparted to the investigated molecule.

While fluorescence microscopy techniques remain the most widely used optical tools for imaging cellular components with high spatial resolution, most fluorescence-based imaging modalities are limited by their requirement for exogenous fluorescent labels if chemical specificity is to be achieved.[1] Due to a similar molecular size observed between many fluorescent labels and the biomolecules with which they are conjugated, the biological activity, cellular localization, and dynamics of molecules can be perturbed.[2] Organic fluorophores have been shown to interfere with binding

Published under an exclusive license by AIP Publishing

kinetics between proteins and their associated receptors,[3] while labeling artifacts and non-specific binding are common problems in the fluorescent study of lipids.[4,5] In addition, the broad emission spectra shown by fluorescent labels limit the potential for multiplex imaging.[6] Moreover, the generation of reactive oxygen species with prolonged fluorophore excitation can induce photobleaching and phototoxic cell damage, limiting imaging over longer timescales.[7]

Vibrational micro-spectroscopy techniques can bridge the gap between spatially resolved imaging and chemical profiling by exploiting vibrations of chemical bonds within a specimen. As these vibrational resonances relate to the mass of the constitutive atoms and the strength of the bonds between them,[8] chemical information can be extracted from samples without the necessity for exogenous labeling. Spontaneous Raman micro-spectroscopy has emerged as a non-invasive optical technique that can be used to determine the chemical composition of endogenous cellular components. However, typical biomolecules have small Raman scattering cross sections (in the range of 10^{-29} cm^2 per vibrational mode, ~14 orders-of-magnitude smaller than typical absorption cross sections of fluorophores[9]). The correspondingly limited flux of Raman scattered photons from biological materials necessitates high excitation powers and long integration times for sufficient image contrast, limiting compatibility with living systems.[10] Furthermore, the fluorescent background, if present, severely interferes with Raman imaging due to the additional shot noise and artifacts arising from separating the Raman signal.

Coherent Raman scattering (CRS) techniques, such as coherent anti-Stokes Raman scattering (CARS), can address the acquisition speed problems associated with spontaneous Raman scattering. In CRS, two incident light fields are used to coherently drive the vibration of identical chemical bonds in the focal volume, with a resonance that is equal to the frequency difference between the two light fields.[11–13] As identical vibrating bonds are driven in phase, the corresponding Raman scattered fields constructively interfere, giving a marked enhancement in a detectable signal compared to spontaneous Raman scattering,[9] enabling fast acquisition at moderate powers. The technique has been widely employed for the label-free study of various biomolecules, including nucleic acids,[14–18] proteins,[19–26] water,[27–29] and lipids[30–39] via excitation of phosphate, amide I, oxygen–hydrogen, and carbon–hydrogen chemical groups, respectively. Hyperspectral CARS, where spatially resolved images are acquired sequentially at multiple vibrational frequencies,[40] offers superior chemical specificity owing to the generation of spectra for each spatial point of an image.[41] Albeit CARS intensity spectra have non-trivial line-shapes due to the interference between the vibrationally resonant and non-resonant parts of the susceptibility, data analysis methods have been developed to retrieve Raman-like spectra.[42–44] Importantly, these have amplitudes that are linear in the concentration of chemical components, aiding interpretation of data and permitting quantitative analyses to be performed.[20]

Raman tags have recently emerged as a labeling strategy that can be used in conjunction with Raman-based imaging techniques to improve chemical contrast.[45] For example, the CH-stretch region of the Raman spectrum in the 2800–3000 cm^{-1} wavenumber range is notoriously congested, thus making the identification of an individual chemical component challenging.[46] Raman tags address this limitation by shifting the position of Raman peaks into regions where the prevalence of resonances is at a minimum or where they are absent altogether, e.g., the cell-silent region (1800–2600 cm^{-1}). One such tag is deuterium, the heavier isotope of hydrogen. Selective replacement of hydrogen with deuterium has been utilized for visualization of proteins,[24,25] carbohydrates,[47] and lipids[48–50] within cell systems, owing to the generation of peaks corresponding to C–D bond resonances within the cell-silent region of the Raman spectrum. This enables selective detection of Raman-tagged molecules against the mixed chemical background of a cell. Unlike bulky fluorescent labels, deuterium incorporation introduces minimal structural change from the endogenous forms of the chemicals of interest.[51]

We have previously developed a data analysis algorithm called "Factorization into Susceptibilities and Concentrations of Chemical Components (FSC^3)",[20,21] which provides an unsupervised and unbiased quantitative chemical analysis of hyperspectral CARS datasets. The analysis generates spatially resolved concentration maps of separate components, in vol/vol concentrations, with the associated Raman susceptibility spectra of each component, in units relative to a reference medium, e.g., glass, without prior knowledge. Our previous work[31,32,52,53] has showcased the application of the FSC^3 analysis to hyperspectral CARS images acquired from a custom-built second-generation multiphoton microscope dedicated to biological studies, revealing the spatial distribution of components such as water, proteins, lipids, and DNA in fixed[32,52] and living cells[31] and distinguishing phase-separated lipid domains in model membrane systems.[53] Notably, in these previous hyperspectral CARS studies, we did not explore the use of Raman tags. Very recently, we studied the quantitative CRS susceptibility of deuterated compounds,[54] showing that the susceptibility of the stretch vibrations approximately scales with their frequency under isotope substitution.

Here, we have investigated HeLa cells cultured in media containing non-deuterated and deuterated isoforms of three fatty acids exhibiting the increasing degree of unsaturation, namely, the monounsaturated oleic acid (OA), the biunsaturated linoleic acid (LA), and the triunsaturated linolenic acid (LNA), to examine how the combination of hyperspectral acquisition with Raman tagging strengthens the ability of our quantitative CARS system to identify and distinguish specific fatty acids with subcellular spatial resolution, in absolute vol/vol concentrations, and with no prior knowledge. We show the application of this imaging strategy to quantify lipid uptake and turnover and for non-invasive tracking of cells of interest within mixed populations.

MATERIALS AND METHODS

Lipids

Pure (>95%) oleic acid (OA) (a monosaturated C18:1 molecule with a cis double bond at the ninth carbon), D17-oleic acid (D17-OA) (with 17 deuterium atoms attached to carbons 11–18), linoleic acid (LA) (a biunsaturated C18:2 molecule with two cis double bonds at the ninth and twelfth carbons), D11-linoleic acid (D11-LA) (with 11 deuterium atoms attached to carbons 14–18), α-linolenic acid (LNA) (a triunsaturated C18:3 molecule with cis double bonds at the ninth, twelfth, and fifteenth carbons), and D14-α-linolenic acid (D14-LNA) (with 14 deuterium atoms attached

Published under an exclusive license by AIP Publishing

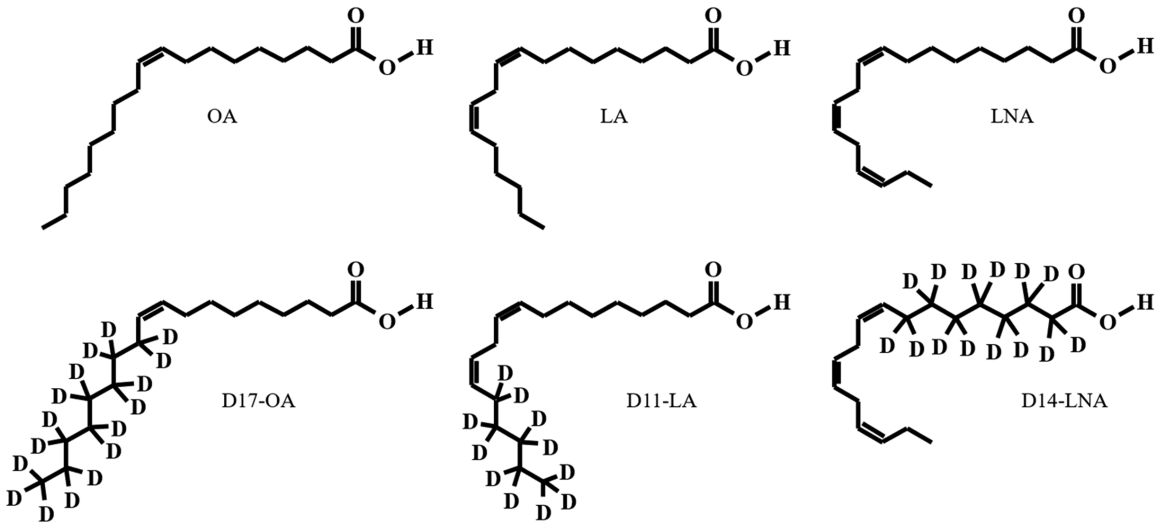

FIG. 1. Chemical structures of the six investigated fatty acid variants generated using the freely available online resource, MolView. OA: oleic acid, D17-OA: D17-oleic acid, LA: linoleic acid, D11-LA: D11-linoleic acid, LNA: α-linolenic acid, and D14-LNA: D14-α-linolenic acid.

to carbons 2–8) were purchased from Cayman Chemical (MI, USA). The chemical structures of each of the investigated fatty acids are shown in Fig. 1.

Cell culture and treatment

Human cervical carcinoma (HeLa) cells (ATCC, UK) were cultured in minimum essential medium (MEM) supplemented with GlutaMAX^{TM} (Life Technologies, UK) and 10% (v/v) fetal bovine serum (FBS) (Life Technologies, UK) directly onto glass coverslips (thickness no. 1.5, 25 mm diameter, PA, VWR International, USA). Following 8 h incubation in MEM + GlutaMAX with 10% FBS, cells were transferred to MEM + GlutaMAX supplemented with fatty acid-free FBS (Biowest, France) to deplete cells of visible lipid droplets. After 18 h incubation, cells were transferred to MEM + GlutaMAX supplemented with lipid-free FBS and a complex of bovine serum albumin (BSA) (Sigma-Aldrich, UK) and the investigated fatty acid at a concentration of 47 μg/ml. Fatty acid–BSA complexes were formed by adapting a published protocol,[55] which involved combining 5% BSA/PBS solutions with 20 mM sodium-fatty acid solutions to form fatty acid–BSA complexes with a final concentration of 1.656 mg/ml. The fatty acid-supplemented media was transferred onto cells within a sterile cell culture hood using a 4 mm diameter, 0.22 μm filter (Corning, USA) and a 2 ml syringe (Becton Dickinson, USA). In each experiment, cells were initially incubated in fatty acid–BSA-supplemented media for an 18 h period. In lipid identification experiments, coverslips were then fixed in a 4% formaldehyde–PBS solution (Affymetrix, UK) for 20 min and mounted onto standard glass microscope slides using a 9 mm diameter, 120 μm thick adhesive imaging gasket (Grace BioLabs, OR, USA) filled with water. In uptake/turnover experiments, cells were exposed to alternative fatty acid–BSA-supplemented media for up to 24 h following the initial 18 h incubation, after which cells were fixed in the same way as above. In cell tracking experiments, after the initial 18 h incubation, cells were detached from their culture dishes and combined to give a mixed population. Cells were then fixed using the same method as above after 8, 16, or 24 h following mixing.

Multimodal CARS microscope configuration

Hyperspectral CARS datasets were acquired using a custom-built multimodal laser scanning CARS microscope, the layout of which has been described in detail in our previous works.[40,56] In short, a single 5 fs Ti:Sa broadband (660–970 nm) pulsed laser (Venteon, Pulse:One PE) was pumped using a Nd:vanadate laser (Laser Quantum, Finesse) at 4.5 W to generate <8 fs pulses with a spectral width of 310 nm at 10% of the maximum intensity at a repetition rate of 80 MHz and with an average output power of 500 mW. A series of dichroic beam splitters were used to separate the transmitted beam into the pump and Stokes components centered at 682 and 806 nm with a bandwidth at 10% of the maximum of 65 and 200 nm, respectively. Spectral focusing through linear chirping of the pump and Stokes beams produced pulses of duration ~1 and 4 ps, respectively, achieving a spectral resolution of 10 cm^{-1}. Hyperspectral CARS data could be acquired over the spectral range, 1200–3800 cm^{-1}, without adjustments to the laser by changing the relative delay time between pump and Stokes pulses. Following recombination, the excitation beams were coupled into a commercial microscope stand (Nikon Ti-U) via a custom-built scanning head. For all work presented here, a 60×, 1.27 NA, 0.17 mm working distance (WD) water immersion objective (Nikon CFI Plan Apochromat IR λS Series, MRD70650) was used with a 1.34 NA, 1.95 mm WD oil condenser (Nikon T-C-HNAO, MEL41410) and a 1× tube lens, permitting high resolution imaging [with a spatial resolution of 0.2 (0.3) μm in-plane and 0.65 (0.9) μm axially, as CARS intensity

Published under an exclusive license by AIP Publishing

(field) full width at half maximum (FWHM)].[57,58] The CARS signal was collected in the forward direction using a photomultiplier tube (PMT) (Hamamatsu H7422-40). The use of double Semrock FF01-593/40 and Semrock FF01-562/40 bandpass filters permitted CARS imaging within the cell-silent (1650–2800 cm^{-1}) and CH-stretch (2600–3700 cm^{-1}) regions of the Raman spectrum, respectively. Hyperspectral CARS datasets were collected within both spectral regions by acquiring in-plane *xy* images over a range of wavenumbers with a step size of 5 cm^{-1}. A pixel size of 70 × 70 nm^2 was used with a pixel dwell time of 100 μs. Non-resonant CARS spectra from glass were recorded under the same excitation and detection conditions and used for normalization to correct for the varying temporal overlap of pump and Stokes pulses and to derive a CARS intensity ratio independent of excitation/detection parameters. For correct quantification of CARS intensity ratios, backgrounds were measured under the same excitation and detection conditions with pump and Stokes pulses out of time overlap and subtracted from the measured CARS intensities prior to data analysis. The microscope was also equipped with differential interference contrast (DIC), which was utilized for selection of regions of interest within samples prior to CARS imaging. DIC imaging was undertaken with the same objective and condenser combination used for CARS, and images were acquired using a CCD camera (Hamamatsu Orca-285). Both in-plane *xy* sample motion and objective focusing in the *z*-direction were motorized [Prior ProScan III controller (V31XYZ), xy stage (H117NN2N), and z drive (PS3H122)].

Spontaneous Raman imaging

Spontaneous Raman spectra were acquired using an in-house-developed confocal Raman micro-spectrometer utilizing the same microscope stand as the CARS instrument described above. A 40×, 0.95 NA, 0.21 mm WD dry objective (Nikon CFI Plan Apochromat IR λS Series, MRD00405) and a 0.72 NA, 12.5 mm WD condenser (Nikon Ti-C-CLWD, MEL56100) were used for acquisition of spectra. The excitation beam from a 532 nm laser (Laser Quantum GEM) was initially passed through an exciter filter (Semrock LL01-532) and coupled into the microscope via a dichroic mirror (Semrock LPD01-532RS). Raman scattering was collected in the epi-direction, filtered with a long pass filter (Semrock BLP01-523R), dispersed using a spectrometer (Horiba Jobin-Yvon iHR550) with a grating of 300 lines/mm blazed at 600 nm, and detected with a CCD camera (Andor Newton DU971N-BV cooled to −60 °C). Horizontal (Thorlabs VA100) and vertical (internal to the spectrometer) slits provided confocality. The spectral resolution was 13 cm^{-1}. All measurements were performed with samples at room temperature. An exposure time of 20 s and an excitation power of ~100 mW at the sample were used.

Brightfield and fluorescence imaging

Brightfield and fluorescence images were acquired using an inverted Olympus IX73 microscope equipped with a Prior Lumen200Pro light source and a CMOS Hamamatsu Camera (ORCA Flash 4.0 V2) and controlled using HCImaging software. A 40×, 0.95 NA, 0.18 mm WD dry objective (Olympus UPLSAPO Series) was used with a 2 × 2 binning readout, corresponding to a pixel size of 0.325 μm. During tracking experiments, cells were labeled with Dextran-Alexa488 (ThermoFisher Scientific, UK) at 100 μg/ml for 2 h and imaged using a filter set containing a 490 nm center, 20 nm bandwidth exciter and a 525 nm center, 36 nm bandwidth emitter.

Data analysis

A detailed description of the applied data processing and analysis procedures can be found in our previous works.[20,21] Hyperspectral CARS images were noise-filtered with a singular value decomposition (SVD) algorithm on the square root of the CARS intensity, retaining only components above noise. CARS intensity ratios were then calculated by dividing the background-corrected CARS intensity by the corresponding non-resonant CARS intensity measured in glass under the same excitation and detection conditions. The phase-corrected Kramers–Kronig (PCKK) method was used to retrieve from the CARS intensity ratio the complex CARS third-order susceptibility (in units of the non-resonant susceptibility of glass[54]), which is linear in the concentration of chemical components. Non-negative matrix factorization applied to the imaginary part and the average real part of the susceptibility with an additional concentration constraint (FSC^3) was used to obtain susceptibility spectra of separate chemical components and their volume concentrations in vol/vol units. FSC^3 is unsupervised and thus does not require prior knowledge of the spectra of chemical components, instead it uses random initial guesses. The number of components used in the factorization can be determined in two ways: automatic determination where the number of components is defined when the spectral error calculation for the dataset falls within defined parameters, or with a supervised approach, where the user runs a series of factorizations with an increasing number of components and determines the optimal number of components as the minimum value required to provide unique spatial and spectral features while no significant improvement in the factorization error is observed upon increasing the number of components. In both instances, the optimal number of components is based purely on the factorization error rather than any specific spectral shape, which is determined in an unsupervised way. In this work, we have adopted the second approach. Throughout this study, we applied the algorithm to multiple datasets simultaneously rather than obtaining spectra for each image stack individually. This allowed us to identify common spectra across all hyperspectral image stacks and directly compare the chemical composition of samples.

RESULTS AND DISCUSSION

Raman characterization of lipids

Hyperspectral CARS imaging combined with the unsupervised FSC^3 data analysis permits the identification of chemical components, in terms of Raman-like susceptibility spectra and spatially resolved concentration maps, without prior knowledge. Spontaneous Raman spectra from pure chemical species can therefore provide a reference for interpretation of the chemical information obtained by FSC^3 inside cells. For this reason, pure droplets of each investigated fatty acid derivative (mounted between glass and surrounded by air) were used to acquire spontaneous Raman spectra, which are shown in Fig. 2 together with their well-characterized

Published under an exclusive license by AIP Publishing

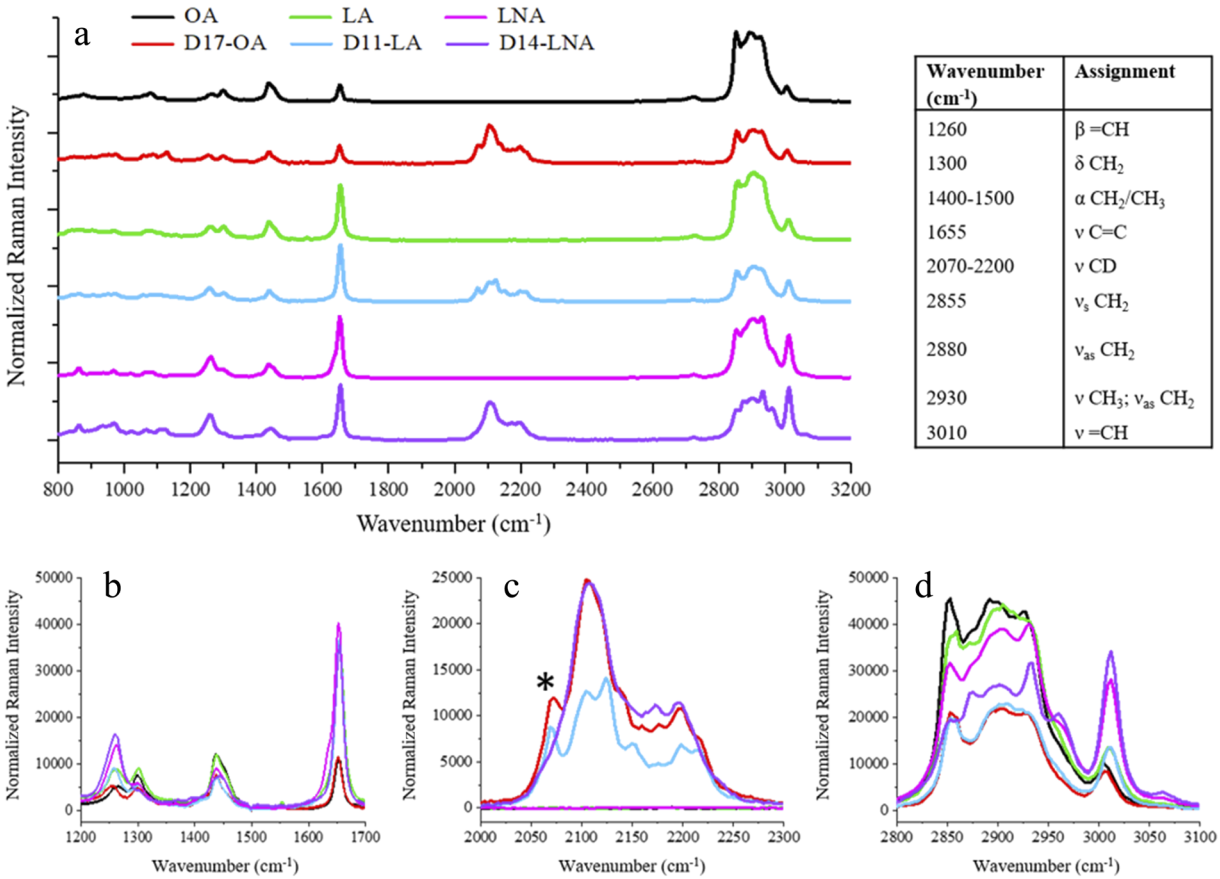

Wavenumber (cm^{-1})	Assignment
1260	β =CH
1300	δ CH_2
1400-1500	α CH_2/CH_3
1655	ν C=C
2070-2200	ν CD
2855	ν_s CH_2
2880	ν_{as} CH_2
2930	ν CH_3; ν_{as} CH_2
3010	ν =CH

FIG. 2. Spontaneous Raman spectra and vibrational mode assignments for the investigated fatty acids. Full spectra are shown (a) with a spectral range of 800–3200 cm^{-1} and are vertically shifted with respect to each other for clarity. Spectra are also shown with the reduced spectral ranges of 1200–1700 cm^{-1} (b), illustrating fingerprint region peaks, 2000–2300 cm^{-1} (c), targeted around the CD-stretch peaks centered at ~2100 cm^{-1} within the silent region of the spectrum, and 2800–3100 cm^{-1} (d), displaying characteristic CH-stretch peaks. Spectra are transposed directly from full spectra but are not vertically shifted, enabling inclusion of Raman intensity values. The asterisk indicates the 2070 cm^{-1} CD-stretch peak, which is present in D17-OA and D11-LA spectra but absent in the D14-LNA spectrum. OA: oleic acid, D17-OA: D17-oleic acid, LA: linoleic acid, D11-LA: D11-linoleic acid, LNA: α-linolenic acid, and D14-LNA: D14-α-linolenic acid; color attributions apply to all spectra within the figure. Symbols for vibrational modes: ν—stretching (further categorized into ν_s—symmetric stretch and ν_{as}—asymmetric stretch) and β—bending/deformation (further categorized into α—scissoring and δ—twisting).

vibrational peak attributions.[59–62] To permit relative comparison of peak amplitudes, spectra from deuterated/non-deuterated fatty acids were scaled so that the pairs had equal 1655 cm^{-1} peak areas and the non-deuterated compounds had equal 2750–3100 cm^{-1} peak areas. By using a combination of both 1655 and 2750–3100 cm^{-1} peak areas, all six of the investigated fatty acid derivatives could be normalized against one another, and relative comparisons between different peaks were possible. A linear baseline subtraction was also applied between the endpoints in each spectrum.

Peaks at 1300 cm^{-1} and between 1400 and 1500 cm^{-1} [Fig. 2(b)] correspond to twisting of CH_2 groups and scissoring motions of CH_2/CH_3 groups, respectively. For each of the investigated fatty acids, the CH_2 twist peak divides into two peaks at 1260 and 1300 cm^{-1}, attributed to =CH bending and CH_2 twisting, respectively, due to unsaturation within the acyl chain. For LNA, the peak at 1260 cm^{-1} appears larger than the peak at 1300 cm^{-1} due to a greater degree of unsaturation in comparison to both OA and LA, and in D14-LNA, the 1300 cm^{-1} peak is completely overwhelmed due to both the high degree of unsaturation and the selective replacement of CH_2 groups with CD_2 groups. Similarly, the C=C stretch peak at 1655 cm^{-1} shows increasing intensity with the increasing degree of unsaturation. Differences are also apparent when comparing each of the deuterated fatty acids with their non-deuterated counterparts: the peaks at 1300 and 1400–1500 cm^{-1} show a lower intensity in all deuterated fatty acids due to fewer CH_2 and CH_3 groups present within their chemical structures following deuterium incorporation within the acyl chain. Fig. 2(d) shows an overlay of the CH-stretch peaks for each of the investigated fatty acids with a reduced spectral range, enabling clear visualization of spectral lineshapes. The CH-stretch region peaks at 2855, 2880, and 2930 cm^{-1}

Published under an exclusive license by AIP Publishing

show reduced intensity (and total area) in the spectra from each of the deuterium-containing fatty acids compared to those from the unlabeled parent molecules owing to a reduced total number of carbon–hydrogen bonds following deuterium incorporation. The =CH-stretch peak at 3010 cm^{-1} increases in intensity as the degree of unsaturation increases.

Raman spectra from the deuterated fatty acid isoforms show a CD-stretch peak centered around 2100 cm^{-1}, as shown in Fig. 2(c), where CD-stretch peaks from each of the deuterated fatty acids are overlaid with a reduced spectral range. As is observed in the CH-stretch region, the CD-stretch peaks show overlap between vibrational resonances, making the assignment of peaks challenging. The chemical structures for the deuterated fatty acids, shown in Fig. 1, reveal that while D17-OA and D11-LA possess a deuterated methyl group (CD_3) at the 18th carbon, D14-LNA contains deuterium at carbons 2–8 at the carboxylic acid end of the acyl chain and thus does not possess a comparable CD_3 group. The acquired Raman spectra therefore suggest that the peak at 2070 cm^{-1} [shown by an asterisk in Fig. 2(c)] corresponds to CD_3-related resonances owing to its absence in the D14-LNA spectrum. The main peak at 2100 cm^{-1} and the shoulder around 2200 cm^{-1} are present in spectra from all three of the deuterated fatty acids and are therefore considered to correspond to CD_2 stretching vibrations. These attributions are consistent with recently reported Raman spectra comparing fully deuterated with partially deuterated palmitic acid.[63] An understanding of the peak attributions within the Raman spectra from each investigated fatty acid is necessary for the interpretation of CARS hyperspectral datasets when transitioning into cellular systems. Comparison between the CARS spectra generated by hyperspectral cellular imaging and the spontaneous Raman spectra from pure fatty acid samples permits evaluation of the ability of FSC^3 to derive specific spectral features and assessment of any loss of chemical specificity.

Hyperspectral CARS and FSC^3 data analysis for intracellular visualization of deuterium-labeled fatty acids

Here, we investigated the ability of our quantitative hyperspectral CARS imaging and analysis strategy to identify chemical components corresponding to C–D bond vibrations, thus enabling the specific visualization of deuterium-labeled fatty acids and their concentration, within a cell. Figure 3 shows the spatial and spectral outputs of the unsupervised FSC^3 analysis applied to cytosolic lipid droplets from HeLa cells treated with each of the investigated fatty acids. Cells treated with deuterium-labeled and unlabeled isoforms of the same fatty acid were analyzed together so that common spectra across both groups were retrieved, thus enabling a direct comparison of lipid droplet composition. The main spectral components within the hyperspectral datasets were identified and displayed as spatial concentration maps with representative component spectra retrieved over the range of 1900–3100 cm^{-1}, showing bands corresponding to CD- and CH-stretch vibrations. Two separate scans were performed, one over the spectral range of 1800–2700 cm^{-1}, using a Semrock FF01-593/40 bandpass filter, and the other over the spectral range of 2700–3200 cm^{-1} using a Semrock FF01-562/40 bandpass filter. These two spectra were then joined together, and PCKK was applied across the combined spectral range (1800–3200 cm^{-1}). Six separate chemical components were considered in the factorization algorithm, which allowed the separation of chemical species corresponding to water, protein, unlabeled lipid, and deuterium-labeled lipid and two less well-defined components that did not provide additional chemical information and instead were likely artifacts generated when joining together cell-silent region and CH-stretch region spectra and applying PCKK (Fig. 1 in the supplementary material). Concentration errors and spectral errors for this factorization are provided in Fig. 2 in the supplementary material. DIC images were acquired for the visualization of whole cells and selection of lipid-rich regions for hyperspectral CARS imaging.

For each of the deuterated/non-deuterated fatty acid pairings, chemical components were assigned consistently based on the spatially resolved concentration maps and the retrieved susceptibility spectra. Component 1 was attributed to the aqueous medium surrounding the lipid droplets, consisting primarily of water. Water does not typically show peaks over the selected spectral range and produces a broad peak at ~3200 cm^{-1}. The attribution of Component 1 to water was supported by spatial localization of the signal outside the observed lipid droplets, with the strongest signal being observed extracellularly, where only water was present. Component 2 was attributed to protein, with a peak at ~2950 cm^{-1}, and an observed signal within cytoplasmic cellular regions and at the periphery of the cytosolic droplets. Component 3 was attributed to unlabeled fatty acids owing to signal localization within lipid droplets and a retrieved spectrum showing a C–H stretch band at 2800–3000 cm^{-1} but no C–D stretch band at ~2100 cm^{-1}. We note that cytosolic droplets of cells treated with deuterium-labeled fatty acids also exhibit Component 3 due to the presence of C–H bonds and ongoing fatty acid synthesis; however, the concentration of this component is larger in cells treated with unlabeled fatty acid. Component 4 was attributed to deuterium-labeled fatty acids, showing a CARS signal localized within droplets and a CD-stretch band at ~2100 cm^{-1} within its retrieved spectrum. The signal was only observed for this component within droplets from cells treated with deuterium-labeled fatty acid. A band at 2800–3000 cm^{-1}, corresponding to C–H stretch vibrations, was also observed in the retrieved spectrum for Component 4 due to C–H bonds remaining in the incompletely deuterated fatty acids. As was observed in the Raman spectra in Fig. 2, the shape of the CD-stretch band within the retrieved spectra for Component 2 varied between D17-OA-, D11-LA-, and D14-LNA-treated cells. A sub-peak at 2070 cm^{-1} was observed for D17-OA- and D11-LA-treated cells [Figs. 3(a) and 3(b)], while a corresponding peak was absent from D14-LNA-treated cells [Fig. 3(c)], once again suggesting that this sub-peak relates to the CD_3 stretch.

These results demonstrate the capability of our hyperspectral CARS imaging system combined with the FSC^3 analysis to distinguish deuterium-labeled fatty acids from a chemically complex cellular background, generating susceptibility spectra in good agreement with reference Raman spectra, without prior knowledge, and providing the corresponding quantitative concentration maps. Importantly, we have generated spectra that span an extended Raman range, incorporating both cell-silent and CH-stretch regions. This enabled us to separate partially deuterated molecules from their non-deuterated analogs. Had we used a spectral range covering either C–D or C–H peaks individually, as is commonly performed

Published under an exclusive license by AIP Publishing

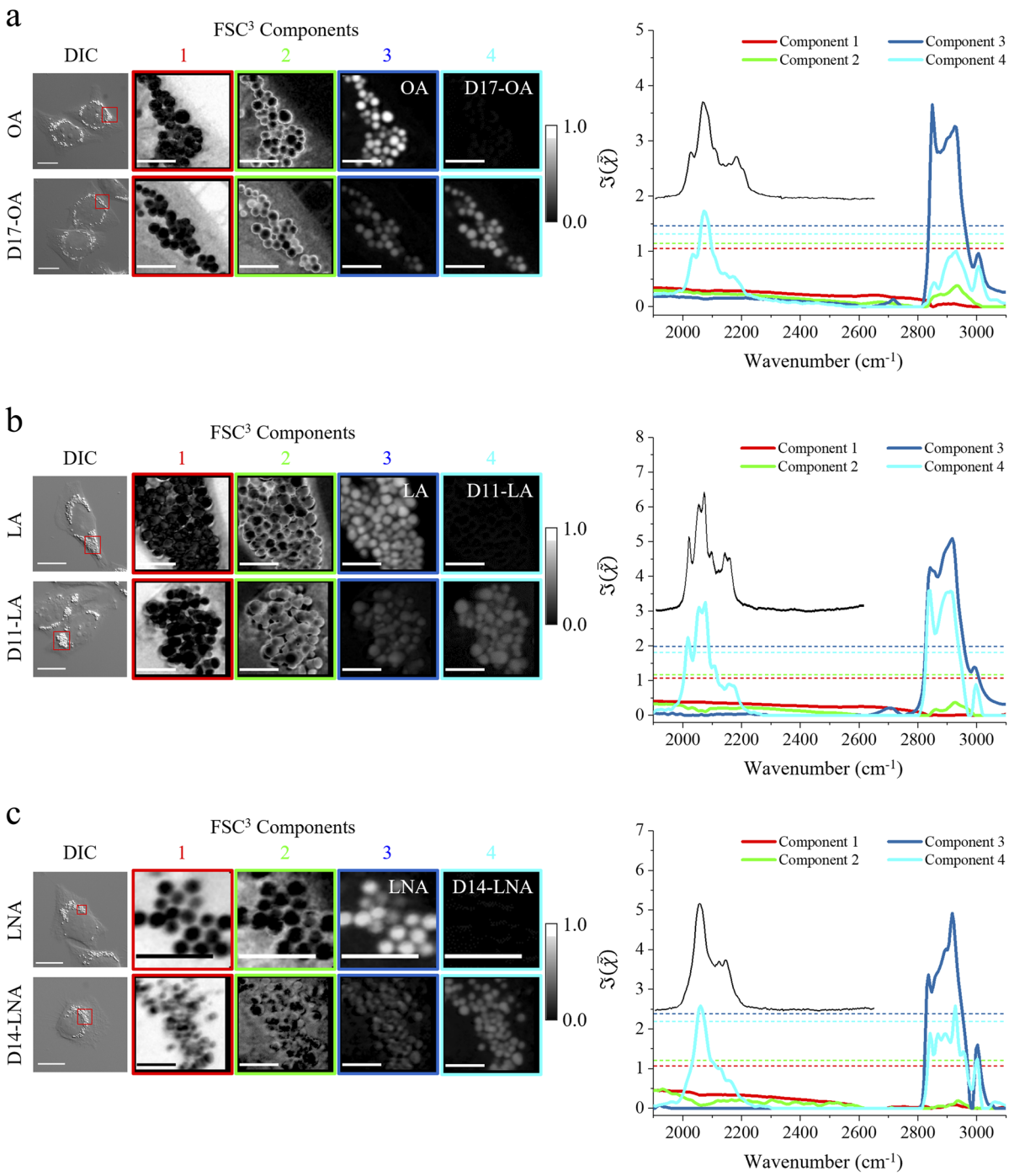

FIG. 3. Spatial and spectral outputs from an unsupervised FSC^3 analysis of hyperspectral CARS datasets for deuterated fatty acid-treated HeLa cells, targeting both CD- and CH-stretch peaks (1900–3100 cm^{-1}). The chemical composition of lipid droplets is directly compared between OA-treated and D17-OA-treated cells (a), LA-treated and D11-LA-treated cells (b), and LNA-treated and D14-LNA-treated cells (c). For each of the deuterated/non-deuterated pairings, concentration maps identify and spatially resolve four components that are chemically specified by their representative CARS susceptibility spectra (imaginary part), $\Im(\tilde{\chi})$. Average real parts of the susceptibility are also shown as horizontal dashed lines. Components are attributed to (primarily) water (Component 1), protein (Component 2), non-deuterated fatty acid (Component 3), and deuterated fatty acid (Component 4). Volume concentrations are given using a grayscale 0–1 in vol/vol units as indicated. Raman spectra from pure lipids (black) are overlaid (vertically shifted) for direct comparison with retrieved spectra for deuterated fatty acid components. DIC images show whole cells and the lipid-rich regions selected for hyperspectral CARS acquisition. Scale bars are 20 μm in DIC images and 4 μm in FSC^3 images.

Published under an exclusive license by AIP Publishing

when utilizing isotope labels in Raman and CRS studies, the generation of both C–D and C–H signals by the partially deuterated molecules would have made their separation from non-deuterated molecules challenging.

FSC^3 data analysis for quantitative visualization of deuterium-labeled fatty acid uptake and turnover within lipid droplets

Having demonstrated the ability of our CARS system and subsequent FSC^3 analysis to identify specific deuterium-labeled fatty acids within a complex cellular environment, we next investigated the applicability of our imaging strategy for quantifying the corresponding changes in the intracellular lipid concentration. To observe the uptake and storage of fatty acids into lipid droplets, HeLa cells were first incubated with unlabeled LA to enable lipid droplet formation before the LA-containing growth medium was replaced with D11-LA-containing medium, and changes in CH- and CD-stretch were assessed. To investigate the time scale over which D11-LA was mobilized from cytosolic droplets, HeLa cells were initially incubated in D11-LA-containing growth medium before replacement with LA-containing medium, thus reversing the order of events from the uptake experiment. Cell samples were fixed at 8, 12, 16, and 24 h time-points following the exchange of media, and a 0 h sample was fixed without exposure to the replacement media. Hyperspectral CARS datasets were acquired from droplet-containing cellular regions, and an unsupervised FSC^3 analysis was applied across all time-points simultaneously to identify common chemical components corresponding to deuterated and non-deuterated LA, with spatial and spectral FSC^3 profiles shown in Fig. 4. Hyperspectral CARS datasets were acquired from intracellular regions of single cells containing a minimum of 15 lipid droplets, and a different cell was imaged at each time-point. An unsupervised FSC^3 analysis was then applied across all time-points simultaneously to identify common chemical components corresponding to deuterated and non-deuterated LA, with spatial and spectral FSC^3 profiles shown in Fig. 4. To reduce overall acquisition time, data collection was performed over the spectral range of 1900–3100 cm^{-1} using only the cell-silent region-specific FF01-593/40 bandpass filter. Although this produced a distorted CH-stretch peak shape with reduced spectral resolution, the generated CH-stretch signal was still sufficient to determine the relative concentration of C–H bonds within cellular lipid droplets. In addition, the generated spectrum for Component 2, showing a typical protein peak at 2950 cm^{-1}, was still sufficient to separate the protein signal from water and lipid signal within the spatial images despite the use of a single filter. PCKK was applied over the whole spectral range of 1800–3100 cm^{-1}.

Seven separate components were considered in the factorization algorithm to enable the identification of chemical species corresponding to water, protein, D11-LA, and LA. Three less well-defined components were also identified, but despite containing some chemical information, these components were more difficult to assign to a specific molecule due to the low signal to noise spectra and inconsistent spatial images (Figs. 3 and 4 in the supplementary material). These three components did not provide additional chemical species to those already identified in Components 1–4 and instead appeared to show variations of the lipid peaks, likely separated from the main lipid components due to small changes in the z-position during image acquisition. The signal observed at the edges of droplets also suggests that some of these components may have corresponded to artifacts generated by sample motion in x and y directions during image acquisition. When less than seven components were considered, retrieved spectra corresponding to D11-LA and LA could not be separated. Figure 5 in the supplementary material shows the concentration and spectral errors for the factorization. Notably, the spectral profile of the retrieved CARS susceptibility for D11-LA is once again in good agreement with its reference Raman spectra, highlighting the high degree of accuracy with which FSC^3 analysis can identify and separate chemical components despite an absence of prior knowledge and a chemically complex intracellular environment.

Figure 4 shows quantitative changes in identified D11-LA and LA components with the exposure of cells to D11-LA over a 24 h period [Fig. 4(a)] and for 24 h following the removal of D11-LA from growth media [Fig. 4(b)]. The 0 h time-point in the LA to D11-LA treatment group shows no spatially resolved CD-stretch component, indicating the absence of D11-LA, while a strong non-deuterated LA component is present within lipid droplets. Following media exchange, the D11-LA component increases until the 16 h time-point, indicating the uptake and storage of D11-LA into lipid droplets. However, from 16 to 24 h, the concentration of the D11-LA component inside lipid droplets decreases, which may be indicative of cells depleting their growth medium of deuterated lipid and beginning to turn over the deuterated lipid stored within their droplets. On the other hand, the LA component increases within the droplets, suggestive of cells synthesizing and storing non-deuterated lipid rather than relying on the accumulation of deuterated lipid from growth media. It should be noted that these results were obtained from a single experiment with no replicates performed, given that the purpose of the study was to evaluate whether FSC^3 analysis could effectively study dynamic changes in the deuterium-labeled biomolecule concentration. However, we highlight this interesting observation as further investigation may be warranted in the future, focusing specifically on lipid metabolism over extended time periods.

The 0 h time-point in the D11-LA to LA treatment group shows a strong CD-stretch component corresponding to D11-LA stored within cellular lipid droplets. A decrease in the CD-stretch signal over the 24 h period indicated the mobilization of D11-LA from lipid droplets, and the increased CH-stretch signal suggested the replacement of the stored D11-LA with the LA provided within the growth medium. It should also be noted that the size of each of the imaged droplets was larger than the 0.2 μm spatial resolution of the 1.27 NA objective used.

Changes in deuterated and non-deuterated lipid components were quantified using our previously published method.[31] Regions containing only lipid droplets were manually selected from spatially resolved FSC^3 images, and the integrated concentrations of the D11-LA and LA components were calculated over the droplet area. The integrated D11-LA and LA component concentrations were then divided by the total integrated lipid concentration (D11-LA and LA components combined) to give the relative D11-LA and LA content per droplet. The resulting relative D11-LA and LA concentrations were plotted against droplet size. Figure 5 presents the changes in the fatty acid concentration within each droplet from

Published under an exclusive license by AIP Publishing

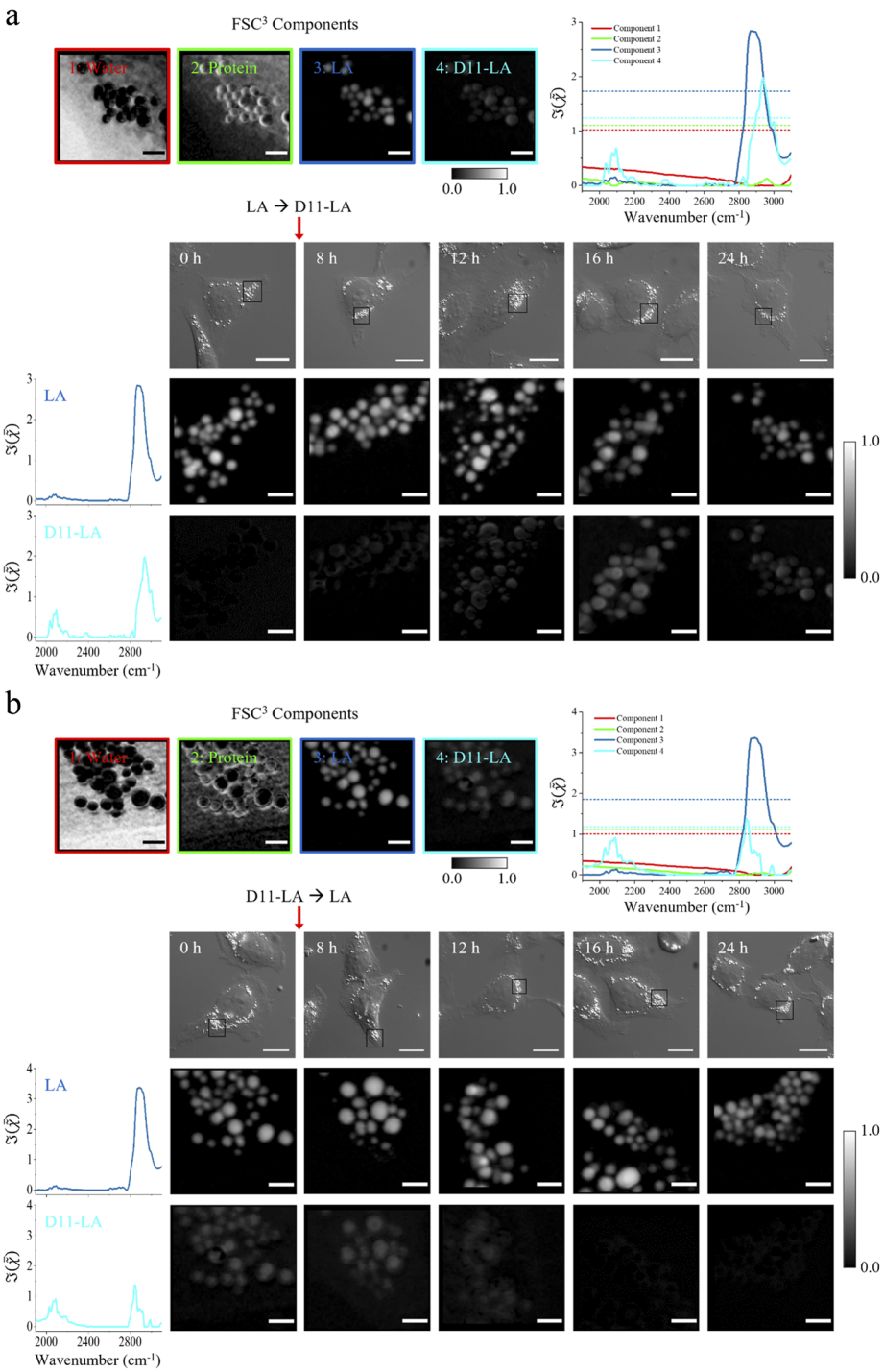

FIG. 4. FSC^3 analysis of D11-LA uptake and storage into (a) and turnover from (b) cytosolic lipid droplets. Droplet-containing cellular regions were imaged by hyperspectral CARS over the spectral range of 1900–3100 cm^{-1}, incorporating CD- and CH-stretch peaks. Spatially resolved images and associated spectra showing the phase-retrieved imaginary part of the normalized CARS susceptibility, $\Im(\tilde{\chi})$, are displayed. The average real parts of the susceptibility are also shown as horizontal dashed lines. Components were identified corresponding to (primarily) water, protein, LA, and D11-LA (an example from a single time-point is shown for each treatment group), and changes in LA and D11-LA components are shown over a 24 h period. The full volume concentration range across images from all time-points is given by the grayscale values. DIC images show whole cells and the droplet-containing regions selected for hyperspectral CARS acquisition. Droplets were analyzed from a single region of a single cell at each time-point, and at each time-point, a different cell was studied. Scale bars show 20 μm in DIC images and 2 μm in FSC^3 images.

Published under an exclusive license by AIP Publishing

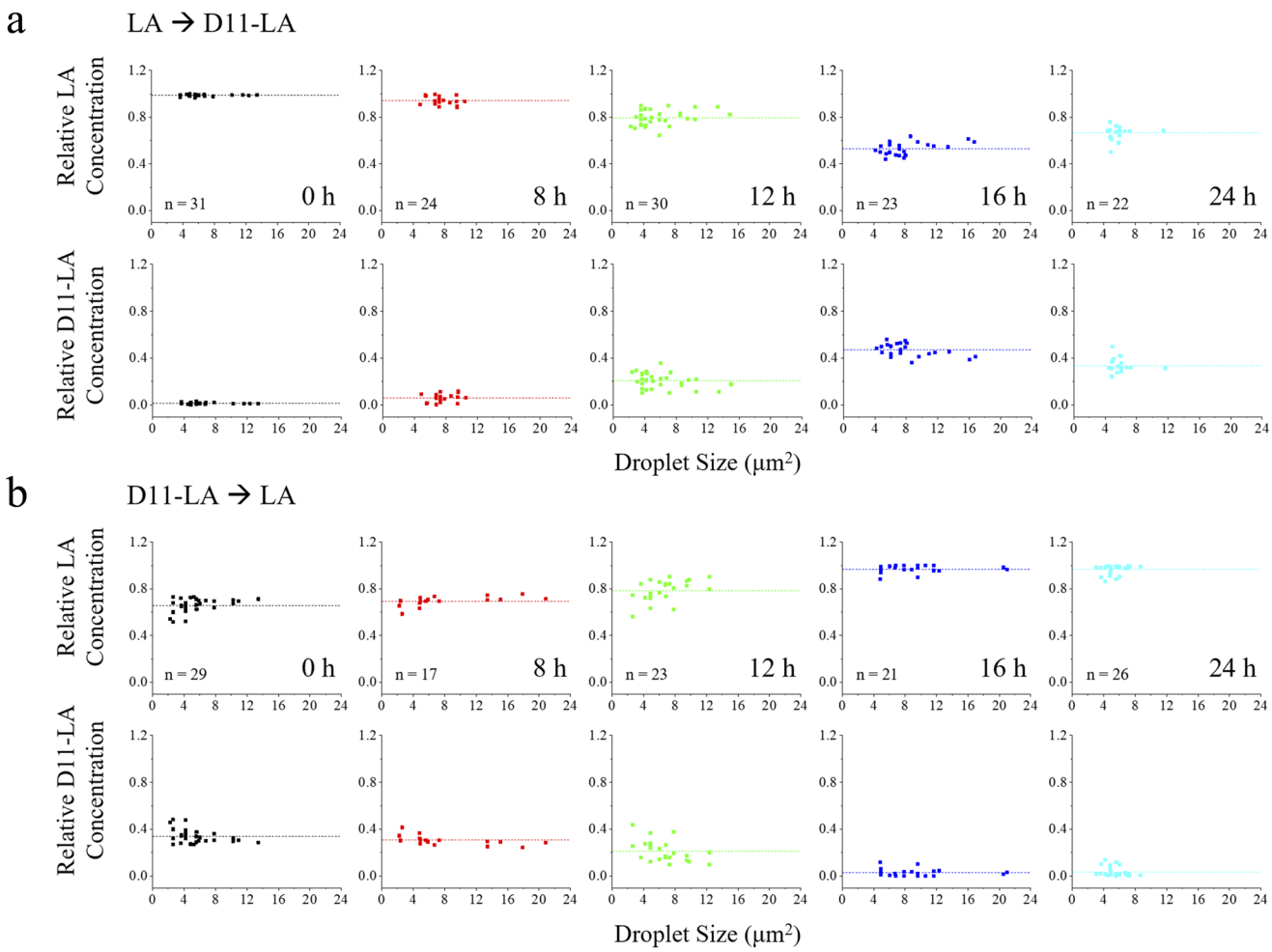

FIG. 5. (a and b) Relative concentrations for the identified LA and D11-LA FSC^3 components shown in Fig. 4. Concentrations are plotted against droplet size for all droplets within each image. n = number of droplets analyzed.

the spatial images in Fig. 4, with each datapoint corresponding to a specific lipid droplet in each intracellular region from separate single cells for each time-point. A different cell was studied at each time-point, and the total number of droplets analyzed ranged from 17 to 31.

With exposure to D11-LA-containing media over a 24 h period, the mean relative D11-LA concentration across all droplets increased from 0.01 to 0.48 over the first 16 h before decreasing to 0.33 at 24 h. With removal of D11-LA from growth media, the mean relative D11-LA concentrations across all droplets decreased from 0.34 to 0.03 over the 24 h period, while the relative concentration of the non-deuterated LA component increased, demonstrating the mobilization of D11-LA from droplets and replacement with LA. The observed change in the LA/D11-LA ratio was independent of droplet size. Importantly, even within dynamic uptake/turnover experiments, such as that described above, FSC^3 is still able to accurately identify a specific deuterated fatty acid, in this case D11-LA, within a chemically complex environment based solely on its CD peak shape.

Deuterium-labeling for non-invasive cell tracking

Building from the demonstration that the FSC^3 analysis can quantitatively distinguish cells treated with deuterium-labeled lipids from those treated with unlabeled lipids, we investigated the possibility of utilizing the storage of deuterium-labeled fatty acids within droplets for non-invasive labeling and quantitative tracking of cells within a mixed population. For this purpose, we conducted a proof-of-concept experiment where a set of HeLa cells (population a) was treated with D11-LA and a second set (population b) was treated with LA before cells were detached from their culture dishes and combined to give a mixed population [Fig. 6(a)]. Subsequent hyperspectral CARS imaging and FSC^3 data analysis of cellular lipid droplets enabled the identification and quantification of the

Published under an exclusive license by AIP Publishing

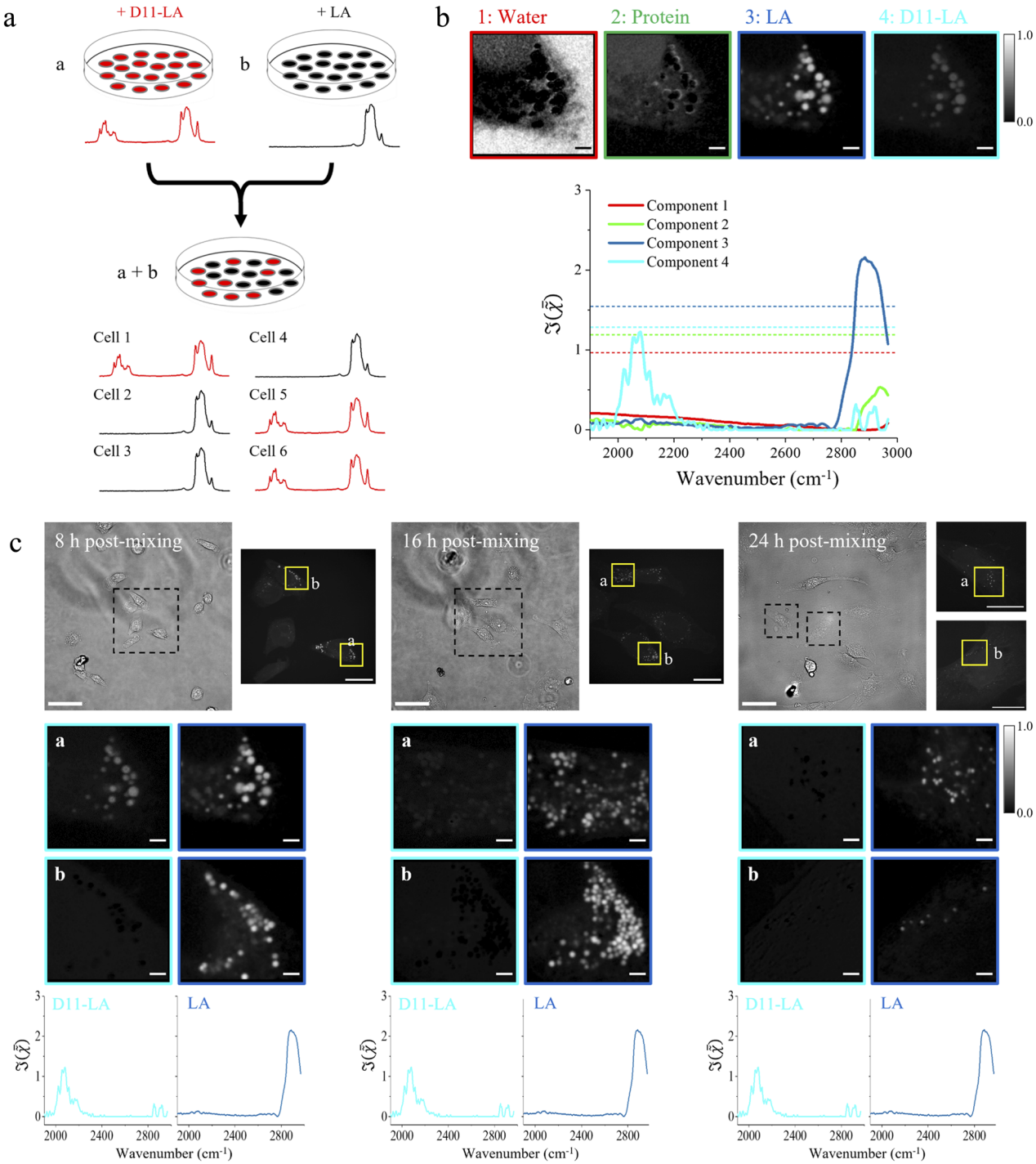

FIG. 6. Overview of non-invasive cell tracking through the FSC^3 analysis of lipid droplet composition (a) and evidence for the potential application of deuterium-labeled lipid visualization for lineage tracking at 8, 16, and 24 h post-mixing of populations [(b) and (c)]. Hyperspectral datasets were acquired from the cellular regions indicated by yellow boxes over the spectral range of 1900–3000 cm^{-1}, and FSC^3 was applied across all samples to identify chemical components corresponding to water, protein, LA, and D11-LA within the field of view. The D11-LA component was then utilized to distinguish between cells within the mixed populations. Spectra show the phase-retrieved imaginary part of the normalized CARS susceptibility, $\Im(\tilde{\chi})$, and the volume concentration range is shown on a grayscale. Brightfield images at 40× magnification provide larger fields of view, showing cells within the mixed populations. Single wavenumber CARS images at 2850 cm^{-1} show whole cells and the droplet-containing regions selected for hyperspectral CARS acquisition. Scale bars show 50 μm in brightfield images, 20 μm in whole-cell images, and 2 μm in FSC^3 images.

Published under an exclusive license by AIP Publishing

CD-stretch component, which was utilized to distinguish between cells from both original populations. HeLa cells were fixed and imaged at 8, 16, and 24 h post-mixing of cell populations, and as previously described, FSC^3 was applied to samples across each of the three time-points simultaneously to identify and spatially resolve common chemical components. Similar to the section titled "FSC^3 data analysis for quantitative visualization of deuterium-labeled fatty acid uptake and turnover within lipid droplets," acquisitions were performed over the spectral range of 1900–3000 cm^{-1} using only the cell-silent region-specific FF01-593/40 bandpass filter, which again produced a distorted CH-stretch peak shape with reduced spectral resolution. However, as the CH-stretch peak was only required to separate LA-treated and D11-LA-treated cells, a high spectral resolution was not necessary. To permit accurate separation of LA-treated and D11-LA-treated cells, it was also necessary to identify and isolate the protein signal from the lipid and water signal. As in Fig. 4, the distortion of the peak shape did not prevent a protein component from being identified despite the retrieval of only a part of the peak, with Component 2 showing a strong signal localized to the protein-rich nuclear region of the cell.

Six components were used in the factorization algorithm to enable the identification of chemical species corresponding to water, protein, D11-LA, and unlabeled LA, the spatial and spectral profiles of which are shown in Fig. 6(b). Two further components were also identified, which were less well-defined in their chemical attributions (Fig. 6 in the supplementary material). The first of these components appeared to also show the protein signal based on its spatial distribution; however, the line-shape of the retrieved spectrum was less representative of protein, while the second of these components appeared to represent the unlabeled lipid, with the signal present within some lipid droplets but not others, suggestive of small changes in the z-position during image acquisition. When less than six components were used, retrieved spectra corresponding to D11-LA and LA were not separated. Figure 7 in the supplementary material shows the concentration and spectral errors for the factorization. LA and D11-LA components retrieved from HeLa cells at 8, 16, and 24 h post-mixing of cell populations are shown in Fig. 6(c), with the presence or absence of D11-LA within lipid droplets enabling cells a and b to be distinguished from one another, hence permitting the assignment of each to its original population. This strategy was shown to be effective for distinguishing cells over a 16 h time period; however, by 24 h, a CD-stretch component could no longer be identified, consistent with the timescale in Fig. 4, and the separation of cells treated with the deuterium-labeled lipid from those treated with the unlabeled lipid could not be achieved. Thus, the applicability of this concept is limited by the timescale of lipid turnover, and its implementation will depend on the timescale over which the cells require tracking.

To confirm that the datasets acquired at each time-poin contained both D11-LA- and LA-treated cells, AlexaFluor488-labeled dextran was applied to the LA-treated cell populations prior to the detachment of cells and mixing of populations. As dextran accumulates in lysosomes, which are maintained through cell division, cells originating from the LA-treated population remained fluorescent throughout the 24 h duration of the experiment, thus providing evidence for the presence of both sets of cells within the imaged fields of view (see Fig. 8 in the supplementary material). To show that the incorporation of the fluorescently labeled dextran did not interfere with the generated CARS signal and hence the line-shape of the retrieved chemical spectra, a comparable mixed cell population was generated without the incorporation of dextran and imaged at 8 h post-mixing (see Fig. 9 in the supplementary material). The spatial and spectral outputs of the water, D11-LA, and LA components within the dextran-free dataset showed strong similarities to those presented in Fig. 6, and the presence or absence of the D11-LA signal could once again be used to separate cells originating from different populations.

CONCLUSION

We have shown that hyperspectral CARS microscopy combined with our in-house-developed quantitative FSC^3 data analysis is able to identify and distinguish three types of specific fatty acids, each in its non-deuterated and deuterated forms, within a HeLa cell, using a blind factorization with no prior knowledge. The analysis retrieves CARS susceptibility spectra with remarkable similarity to the Raman spectra measured in pure lipids and quantifies the concentrations of fatty acids inside cells in physically meaningful vol/vol units. We have also quantitatively monitored changes in the concentration of droplet-based lipids over a 24 h period, hence providing a strategy for the imaging of intracellular lipid metabolism without the necessity for fluorescent labeling. We performed uptake and turnover experiments whereby D11-LA and LA were exchanged, namely, HeLa cells were initially incubated in LA-containing growth medium before replacement with D11-LA-containing medium and vice versa. We observed an uptake of deuterium-labeled fatty acid and storage with an increasing concentration in cytosolic droplets over a 16 h period followed by a decrease from 16 to 24 h. We also found that cells rapidly (<16 h) mobilize fatty acids from their droplet-based stores for utilization in metabolic processes while storing newly presented fatty acid from their growth medium into cytosolic lipid droplets. Moreover, we have shown a strategy for non-invasive tracking of cells of interest within a mixed population. Cells treated with deuterium-labeled fatty acid could be distinguished from other cells within a population for 16 h, although longer tracking times were not possible, consistent with the rapid timescale over which deuterium-labeled fatty acids were mobilized from droplet-based stores and replaced by unlabeled fatty acids. Incorporation of the deuterium into cellular structures with slower turnover times should allow this detection window to be significantly extended.

We initially used two separate bandpass filters to visualize CD- and CH-stretch peaks within spectra from deuterated and non-deuterated fatty acids, allowing each to be clearly separated from one another. For uptake/turnover and cell tracking experiments, we only used the CD-stretch targeted filter, which produced distortions in the CH-stretch peak but reduced overall acquisition time by eliminating the requirement for hardware changes. Increasing throughput is an ongoing challenge within vibrational spectroscopy, and extensive data collection times can often limit cell-based studies. With this in mind, we have demonstrated that even when we reduce experiment time and sacrifice some data quality, FSC^3 data analysis can still accurately identify molecules and quantitatively assess changes in the concentration. We have

Published under an exclusive license by AIP Publishing

previously shown the ability of our analysis strategy to distinguish between fatty acid types based on spectral differences at CH-stretch region wavenumbers.[31] Notably, in this previous study, we performed a *guided* analysis to distinguish monounsaturated from polyunsaturated fatty acid types within cellular systems and observed uptake/turnover, i.e., we used prior knowledge. Here, we have demonstrated that our analysis can accurately identify deuterium-labeled versions of the same fatty acids within cellular systems without any prior knowledge, providing a platform to study changes in the chemical concentration. This unsupervised chemical identification opens the prospect of multiplex imaging using combinations of deuterated and non-deuterated molecules owing to detectable variations in the Raman spectra between similar species (in this case, fatty acids) both in the CH- and CD-stretch spectral regions.

Our work could be expanded to explore the cellular uptake and distribution/accumulation of more than one deuterium-labeled lipid in a multiplex fashion and could permit the observation of dynamic behavior of several molecules within a single, unlabeled cell sample. While several studies have recently applied CRS techniques to visualize the uptake and metabolism of various biomolecules, including lipids,[64] proteins,[23,24,63] glucose,[65] and nucleic acids,[66] multiplexed visualization of uptake/turnover dynamics of more than one molecule is only just emerging and remains to be fully explored. Furthermore, almost all recent uptake and turnover studies have employed stimulated Raman scattering (SRS) microscopy for image generation owing to the absence of the non-resonant background, hence offering improved contrast and SRS spectra that are simpler to interpret. Here, we have demonstrated that hyperspectral CARS imaging combined with the FSC^3 analysis achieves comparable image contrast and provides quantitative information on the concentration of chemical components.

SUPPLEMENTARY MATERIAL

See the supplementary material for the additional unassigned components, the relative concentration and spectral errors from FSC^3 analysis (Figs. 1–7), and data to support cell lineage tracking experiments (Figs. 8 and 9).

ACKNOWLEDGMENTS

D.B. and P.W. acknowledge support from GlaxoSmithKline and the UK BBSRC Research Council (Grant No. BB/N50371X/1). I.P. and D.B. acknowledge support from the MRC (Grant No. MR/R025762/1) via 3DBioNet (Grant No. JX13065). The hyperspectral CARS microscope development was funded by the UK BBSRC Research Council (Grant No. BB/H006575/1) and EPSRC (Grant No. EP/M028313/1). F.M. acknowledges the Ser Cymru II program (Case ID 80762-CU-148) that is funded by Cardiff University and the European Regional Development Fund through the Welsh Government.

AUTHOR DECLARATIONS

Conflict of Interest

The authors have no conflict to disclose.

REFERENCES

[1] P. Watson, A. T. Jones, and D. J. Stephens, Adv. Drug Delivery Rev. **57**, 43 (2005).
[2] F.-X. Theillet, A. Binolfi, T. Frembgen-Kesner, K. Hingorani, M. Sarkar, C. Kyne, C. Li, P. B. Crowley, L. Gierasch, G. J. Pielak, A. H. Elcock, A. Gershenson, and P. Selenko, Chem. Rev. **114**, 6661 (2014).
[3] L. Yin, W. Wang, S. Wang, F. Zhang, S. Zhang, and N. Tao, Biosens. Bioelectron. **66**, 412 (2015).
[4] S. Fukumoto and T. Fujimoto, Histochem. Cell Biol. **118**, 423 (2002).
[5] Y. Ohsaki, Y. Shinohara, M. Suzuki, and T. Fujimoto, Histochem. Cell Biol. **133**, 477 (2010).
[6] H. Yamakoshi, K. Dodo, A. Palonpon, J. Ando, K. Fujita, S. Kawata, and M. Sodeoka, J. Am. Chem. Soc. **134**, 20681 (2012).
[7] V. Magidson and A. Khodjakov, Methods Cell Biol. **114**, 545 (2013).
[8] R. Smith, K. L. Wright, and L. Ashton, Analyst **141**, 3590 (2016).
[9] A. Zumbusch, W. Langbein, and P. Borri, Prog. Lipid Res. **52**, 615 (2013).
[10] N. M. Sijtsema, S. D. Wouters, C. J. De Grauw, C. Otto, and J. Greve, Appl. Spectrosc. **52**, 348 (1998).
[11] J.-X. Cheng and X. S. Xie, J. Phys. Chem. B **108**, 827 (2004).
[12] A. Zumbusch, G. R. Holtom, and X. S. Xie, Phys. Rev. Lett. **82**, 4142 (1999).
[13] I. Pope, W. Langbein, P. Borri, and P. Watson, Methods Enzymol. **504**, 273 (2012).
[14] T. Ichimura, N. Hayazawa, M. Hashimoto, Y. Inouye, and S. Kawata, Phys. Rev. Lett. **92**, 220801 (2004).
[15] F. K. Lu, S. Basu, V. Igras, M. P. Hoang, M. Ji, D. Fu, G. R. Holtom, V. A. Neel, C. W. Freudiger, D. E. Fisher, and X. S. Xie, Proc. Natl. Acad. Sci. U. S. A. **112**, 11624 (2015).
[16] T. Guerenne-Del Ben, Z. Rajaofara, V. Couderc, V. Sol, H. Kano, P. Leproux, and J. M. Petit, Sci. Rep. **9**, 13862 (2019).
[17] A. Pliss, A. N. Kuzmin, A. V. Kachynski, and P. N. Prasad, Proc. Natl. Acad. Sci. U. S. A. **107**, 12771 (2010).
[18] Z. Chen, D. W. Paley, L. Wei, A. L. Weisman, R. A. Friesner, C. Nuckolls, and W. Min, J. Am. Chem. Soc. **136**, 8027 (2014).
[19] A. Karuna, F. Masia, M. Wiltshire, R. Errington, P. Borri, and W. Langbein, Anal. Chem. **91**, 2813 (2019).
[20] F. Masia, A. Glen, P. Stephens, P. Borri, and W. Langbein, Anal. Chem. **85**, 10820 (2013).
[21] F. Masia, A. Karuna, P. Borri, and W. Langbein, J. Raman Spectrosc. **46**, 727 (2015).
[22] J.-X. Cheng, L. D. Book, and X. S. Xie, Opt. Express **26**, 1341 (2001).
[23] L. Wei, Y. Yu, Y. Shen, M. C. Wang, and W. Min, Proc. Natl. Acad. Sci. U. S. A. **110**, 11226 (2013).
[24] L. Wei, Y. Shen, F. Xu, F. Hu, J. K. Harrington, K. L. Targoff, and W. Min, ACS Chem. Biol. **10**, 901 (2015).
[25] L. Shi, Y. Shen, and W. Min, APL Photonics **3**, 092401 (2018).
[26] L. Zhang and W. Min, J. Biomed. Opt. **22**, 066009 (2017).
[27] Y. C. Yu, Y. Sohma, S. Takimoto, T. Miyauchi, and M. Yasui, Sci. Rep. **3**, 2745 (2013).
[28] J.-X. Cheng, S. Pautot, D. A. Weitz, and X. S. Xie, Proc. Natl. Acad. Sci. U. S. A. **100**, 9826 (2003).
[29] E. O. Potma, W. P. De Boeij, P. J. M. Van Haastert, and D. A. Wiersma, Proc. Natl. Acad. Sci. U. S. A. **98**, 1577 (2001).
[30] J. Bradley, I. Pope, F. Masia, R. Sanusi, W. Langbein, K. Swann, and P. Borri, Development **143**, 2238 (2016).
[31] C. Di Napoli, I. Pope, F. Masia, W. Langbein, P. Watson, and P. Borri, Anal. Chem. **88**, 3677 (2016).
[32] C. Di Napoli, I. Pope, F. Masia, P. Watson, W. Langbein, and P. Borri, Biomed. Opt. Express **5**, 1378 (2014).
[33] M. Paar, C. Jüngst, N. A. Steiner, C. Magnes, F. Sinner, D. Kolb, A. Lass, R. Zimmermann, A. Zumbusch, S. D. Kohlwein, and H. Wolinski, J. Biol. Chem. **287**, 11164 (2012).
[34] T. T. Le, S. Yue, and J.-X. Cheng, J. Lipid Res. **51**, 3091 (2010).
[35] R. K. Lyn, D. C. Kennedy, A. Stolow, A. Ridsdale, and J. P. Pezacki, Biochem. Biophys. Res. Commun. **399**, 518 (2010).

Published under an exclusive license by AIP Publishing

[36]J. P. R. Day, G. Rago, K. F. Domke, K. P. Velikov, and M. Bonn, J. Am. Chem. Soc. **132**, 8433 (2010).
[37]H. A. Rinia, K. N. J. Burger, M. Bonn, and M. Müller, Biophys. J. **95**, 4908 (2008).
[38]D. Zhang, M. N. Slipchenko, and J.-X. Cheng, J. Phys. Chem. Lett. **2**, 1248 (2011).
[39]D. Fu, Y. Yu, A. Folick, E. Currie, R. V. Farese, T.-H. Tsai, X. S. Xie, and M. C. Wang, J. Am. Chem. Soc. **136**, 8820 (2014).
[40]I. Pope, W. Langbein, P. Watson, and P. Borri, Opt. Express **21**, 7096 (2013).
[41]G. W. H. Wurpel, J. M. Schins, and M. Müller, Opt. Lett. **27**, 1093 (2002).
[42]M. T. Cicerone, K. A. Aamer, Y. J. Lee, and E. Vartiainen, J. Raman Spectrosc. **43**, 637 (2012).
[43]C. H. Camp, Y. J. Lee, and M. T. Cicerone, J. Raman Spectrosc. **47**, 408 (2016).
[44]R. Houhou, P. Barman, M. Schmitt, T. Meyer, J. Popp, and T. Bocklitz, Opt. Express **28**, 21002 (2020).
[45]W. J. Tipping, M. Lee, A. Serrels, V. G. Brunton, and A. N. Hulme, Chem. Soc. Rev. **45**, 2075 (2016).
[46]C.-Y. Chung, J. Boik, and E. O. Potma, Annu. Rev. Phys. Chem. **64**, 77 (2013).
[47]J. Li and J. X. Cheng, Sci. Rep. **4**, 6830 (2014).
[48]A. Alfonso-García, S. G. Pfisterer, H. Riezman, E. Ikonen, and E. O. Potma, J. Biomed. Opt. **21**, 061003 (2016).
[49]C. Matthäus, C. Krafft, B. Dietzek, B. R. Brehm, S. Lorkowski, and J. Popp, Anal. Chem. **84**, 8549 (2012).
[50]X. S. Xie, J. Yu, and W. Y. Yang, Science **312**, 228 (2006).
[51]S. Hong, T. Chen, Y. Zhu, A. Li, Y. Huang, and X. Chen, Angew. Chem., Int. Ed. **53**, 5827 (2014).
[52]F. Masia, I. Pope, P. Watson, W. Langbein, and P. Borri, Anal. Chem. **90**, 3775 (2018).
[53]A. Nahmad-Rohen, D. Regan, F. Masia, C. McPhee, I. Pope, W. Langbein, and P. Borri, Anal. Chem. **92**, 14657 (2020).
[54]D. Boorman, I. Pope, F. Masia, P. Watson, P. Borri, and W. Langbein, J. Raman Spectrosc. **52**, 1540–1551 (2021).
[55]L. L. Listenberger and D. A. Brown, *Current Protocols in Cell Biology* (John Wiley & Sons, Inc, 2007), pp. 24.2.1–24.2.11.
[56]I. Pope, F. Masia, K. Ewan, A. Jimenez-Pascual, T. C. Dale, F. A. Siebzehnrubl, P. Borri, and W. Langbein, Analyst **146**, 2277 (2021).
[57]I. Pope, L. Payne, G. Zoriniants, E. Thomas, O. Williams, P. Watson, W. Langbein, and P. Borri, Nat. Nanotechnol. **9**, 940 (2014).
[58]A. Karuna, F. Masia, P. Borri, and W. Langbein, J. Raman Spectrosc. **47**, 1167 (2016).
[59]K. Czamara, K. Majzner, M. Z. Pacia, K. Kochan, A. Kaczor, and M. Baranska, J. Raman Spectrosc. **46**, 4 (2015).
[60]J. De Gelder, K. De Gussem, P. Vandenabeele, and L. Moens, J. Raman Spectrosc. **38**, 1133 (2007).
[61]S. P. Verma and D. F. H. Wallach, Biochim. Biophys. Acta, Lipids Lipid Metab. **486**, 217 (1977).
[62]F. Ya, L. Shuang, and X. Da-Peng, Spectrosc. Spectr. Anal. **33**, 3240 (2013); available at https://pubmed.ncbi.nlm.nih.gov/24611378/.
[63]L. Shi, C. Zheng, Y. Shen, Z. Chen, E. S. Silveira, L. Zhang, M. Wei, C. Liu, C. de Sena-Tomas, K. Targoff, and W. Min, Nat. Commun. **9**, 2995 (2018).
[64]C. Stiebing, T. Meyer, I. Rimke, C. Matthäus, M. Schmitt, S. Lorkowski, and J. Popp, J. Biophotonics **10**, 1217 (2017).
[65]R. Long, L. Zhang, L. Shi, Y. Shen, F. Hu, C. Zeng, and W. Min, Chem. Commun. **54**, 152 (2017).
[66]Z. Zhao, Y. Shen, F. Hu, and W. Min, Analyst **142**, 4018 (2017).

Published under an exclusive license by AIP Publishing